UNIVERSITY OF TURKU

Experimental Spatial Heat-Flux Characterization of Cylindrical 21700 Lithium-Ion Cells Using a Transverse Heat Flux Sensor

Mechanical Engineering
Master's Thesis in Engineering and Technology
Faculty of Technology

Author:
Kamil Barcewicz

26.05.2026
Turku

Master's thesis

Subject: Mechanical Engineering
Author: Kamil Barcewicz
Title: Experimental Spatial Heat-Flux Characterization of Cylindrical 21700 Lithium-Ion Cells Using a Transverse Heat Flux Sensor
Supervisor: Dr. Andrey Mityakov
Number of pages: 32 pages
Date: 15.05.2026

Abstract:

Lithium-ion cells used in large battery packs require active thermal management to ensure performance, safety, and cycle life. The design of thermal management systems commonly relies on numerical simulations, where accurate thermal characterization of individual cells is essential. However, verification of cell thermal models remains challenging with conventional temperature-based measurement methods.

This thesis investigates the use of a transverse heat flux sensor (THFS) for direct measurement and spatial mapping of heat flux between a cylindrical 21700 lithium-ion cell and a cooling plate. An experimental setup was developed in which the THFS was integrated into an actively cooled aluminium plate, while thermocouples were used as supporting measurements. Heat flux was measured at three axial positions during electrical cycling under controlled operating conditions.

The results demonstrate a non-uniform axial heat flux distribution, with up to 30% higher local heat flux measured near the cell terminals compared to the middle region of the cell. The observed behaviour is consistent with increased ohmic losses near the current-collector tab regions. In addition, the experimentally estimated total heat transfer showed good agreement with an independent electrical estimate based on internal resistance.

The results indicate that THFS-based measurements provide a viable method for quantitative local thermal characterization of lithium-ion cells. Due to its small thickness, rapid response time, and high sensitivity, the THFS also shows potential for integration into battery systems as an online thermal monitoring tool.

Key words: THFS, transverse heat flux sensor, lithium-ion battery, energy, experimental

Tiivistelmä:

Suurissa akkukokonaisuuksissa käytettävät litiumioniakut edellyttävät aktiivista lämmönhallintaa suorituskyvyn, turvallisuuden ja käyttöiän varmistamiseksi. Lämmönhallintajärjestelmien suunnittelu perustuu perinteisesti numeerisiin simulointeihin, joissa yksittäisten kennojen tarkka lämpötekninen karakterisointi on keskeisessä asemassa. Kennon lämpömallien validointi on kuitenkin edelleen haastavaa perinteisillä lämpötilamittauksiin perustuvilla menetelmillä.

Tässä diplomityössä tarkastellaan poikittaisen lämpövuon anturin (THFS, transverse heat flux sensor) soveltuvuutta sylinterimäisen 21700-litiumionikennon ja jäähdytyslevyn välisen lämpövuon suoraan mittaamiseen sekä sen spatiaaliseen kartoittamiseen. Työssä kehitettiin

kokeellinen mittausjärjestely, jossa THFS integroitiin aktiivisesti jäähdytettyyn alumiinilevyyn, ja täydentävinä mittausmenetelminä hyödynnettiin termopareja. Lämpövuo mitattiin kolmessa aksiaalisessa kohdassa kennon lataus- ja purkusyklin aikana hallituissa käyttöolosuhteissa.

Tulokset osoittivat, että aksiaalinen lämpövuo jakautuu epätasaisesti kennon eri osissa. Kennon napojen läheisyydessä mitattiin paikallisesti enimmillään 30 % suurempi lämpövuo kuin kennon keskiosassa. Havaittu ilmiö on yhdenmukainen sen kanssa, että virrankeräinliuskojen läheisyydessä syntyy suurempia ohmisia häviöitä. Lisäksi kokeellisesti arvioitu kokonaislämmönsiirto vastasi hyvin sisäiseen resistanssiin perustuvaa riippumatonta sähköistä arviota.

Tulosten perusteella THFS-mittaukset tarjoavat käyttökelpoisen menetelmän litiumionikennojen paikallisen lämpöteknisen karakterisoinnin kvantitatiiviseen arviointiin. Anturin ohuus, nopea vasteaika ja herkkyys viittaavat lisäksi siihen, että THFS:llä on potentiaalia toimia osana akkujärjestelmien reaaliaikaista lämpöteknistä seurantaa.

Avainsanat: THFS, poikittaisen lämpövuon anturi, litiumioniakku, energia, kokeellinen tutkimus

Table of contents

1 Introduction

1.1 Background

Rechargeable batteries, particularly lithium-ion cells, have undergone significant development over recent decades. A global transition toward electrification is evident across transportation, industrial machinery, household appliances, and grid-scale energy storage. This development has been accompanied by continuous improvements in key cell metrics, including energy density, cost reduction, cycle life, reliability, and commercial availability.

Although these improvements are typically reported at the cell level, practical implementation in full-scale battery systems requires operation under controlled conditions to fully exploit their performance. Cells are commonly assembled into large packs to increase capacity and power output, which introduces additional challenges in thermal, electrical, and mechanical management.

Designing battery systems at an industrial scale represents a significant engineering challenge. In automotive applications, hundreds of cells must be integrated into a confined volume while maintaining resistance to vibration, mechanical stress, environmental exposure, and large temperature variations. These requirements must be achieved while maintaining cost-effectiveness for commercial viability.

A key limitation in battery pack design is thermal management. For optimal performance and cycle life, lithium-ion cells are typically operated within a temperature range of approximately 15–35 °C. Operation outside this range accelerates degradation mechanisms such as lithium plating, electrolyte decomposition, and solid-electrolyte interphase (SEI) growth, resulting in premature capacity fade.

All lithium-ion cells exhibit internal electrical resistance, typically in the milliohm range, which leads to irreversible heat generation during charge and discharge. At high power levels, this thermal load becomes significant. In high-performance electric vehicles such as the Rimac Nevera, peak thermal losses can reach the order of hundreds of kilowatts under extreme operating conditions [7]. Even in mass-market electric vehicles such as the Tesla Model Y or Volkswagen ID.4, thermal loads can reach several

kilowatts. The magnitude of these thermal effects is illustrated quantitatively in Section 2.3.

High peaks in electrical load generate significant ohmic losses and thermal loads hence the need for active cooling with help of thermal management in modern battery systems.

The design of thermal management systems typically begins with the development of a thermal model of the cell. A geometric representation is constructed in computer aided design software and serves as the basis for finite element method simulations. The accuracy of this model strongly influences the reliability of simulation results. Since the internal structure of lithium-ion cells varies between manufacturers and applications, each cell type must be modelled individually. Consequently, a thermal management solution optimized for one cell may not be directly transferable to cell from another manufacturer despite of similar external geometry.

Validation of thermal models is commonly performed by comparing simulation results with experimental measurements under controlled operating conditions. Conventional approaches include thermocouples and infrared thermography, which provide temperature field measurements used to infer thermal behaviour.

An alternative approach investigated in this work is the use of a transverse heat flux sensor (THFS). Unlike temperature-based methods, the THFS enables direct measurement of heat flux through a surface. The sensor operates based on the transverse Seebeck effect and produces a voltage proportional to the transverse heat flow. Due to its thin form factor and fast dynamic response, it is suitable for integration into confined thermal interfaces and enables high-resolution measurements of transient heat transfer processes. This shifts the measurement approach from temperature field reconstruction to direct heat flux acquisition at the interface level.

In this thesis, the focus is placed on cylindrical lithium-ion cells in the 21700 format (cylinder of 21mm diameter and 70mm height). The objective is to develop a robust method for spatially resolved heat flux mapping across the cell surface, enabling

improved understanding of thermal behaviour and supporting the design of optimized cooling strategies.

1.2 Objective and scope of the thesis

The objective of this thesis is to experimentally evaluate the capability of a transverse heat flux sensor to resolve the spatial distribution of heat transfer from a cylindrical 21700 lithium-ion cell into a cooling plate under controlled operating conditions.

The quantitative study focuses on identifying axial variations in local heat flux at the cell–cooling interface during electrical cycling. Measurements with the THFS give direct numeric results of the heat flux at discrete locations of the cell. Temperature measurements are used as supporting data to verify experimental consistency and to contextualize the measured heat flux distribution.

The results provide experimental insight into local heat transfer distribution from cylindrical lithium-ion cells and can be used in further research to identify optimal cooling strategies, finite element analysis validation, etc.

2 Technical background

This chapter presents the fundamental concepts relevant to lithium-ion battery operation, heat generation, and heat transfer. Degradation mechanisms associated with non-optimal operating temperatures are discussed to highlight the importance of thermal control. In addition, the operating principle of the transverse heat flux sensor (THFS) is introduced, with emphasis on its applicability to thermal characterization of battery cells.

2.1 Li-ion cells

A lithium-ion battery stores energy by a reversible process of intercalation of lithium ions into the anode lattice during charging. Lithium ions pass through the electrolyte from the cathode to the anode, while electrons travel through the external circuit, maintaining charge neutrality. During discharge, the process is reversed: lithium ions migrate back to the cathode, while electrons pass through an external load, releasing their energy as electric work [1, p. 761].

2.1.1 Brief history

The first electrochemical battery was developed by Alessandro Volta in 1800, demonstrating that electric current can be generated from two dissimilar metals in an electrolyte. This device, known as the voltaic pile, was a primary battery and could not be recharged after depletion.

The first rechargeable (secondary) battery was introduced in 1859 by Gaston Planté in the form of the lead–acid battery, which remains in use due to its robustness and low cost [2].

Later developments included nickel–cadmium batteries, invented in 1899 by Waldmar Jungner, which were eventually largely replaced by nickel–metal hydride systems due to higher energy density and reduced environmental impact [3].

Modern energy storage is dominated by lithium-ion batteries, first commercialized by Sony in 1991. Since then, lithium-ion technology has undergone significant

development, with commercially available cells achieving several-fold increases in energy density over the past decades [4].

2.1.2 Current state of the art

Various lithium-ion battery chemistries exist, each optimized for specific performance characteristics. Cells based on nickel–manganese–cobalt (NMC) cathodes and graphite anodes offer high energy density and are widely used in portable electronics and electric vehicles, where low mass and high capacity are critical.

Lithium iron phosphate (LFP) cells use more abundant and lower-cost materials, resulting in reduced energy density but improved cost, safety, and cycle life. These characteristics make them well suited for stationary energy storage systems, where volumetric and gravimetric constraints are less critical.

Lithium-titanate (LTO) cells, typically combined with conventional cathode materials, are characterized by high power capability, long cycle life, wide operating temperature range, and enhanced safety. However, their relatively low energy density and higher cost limit broader adoption [1, p. 758].

In Table 1 presents selected examples of commercially available batteries with high gravimetric energy density across different chemistries. Only cells currently in mass production are included to ensure comparability.

Cell	**Gravimetric energy density (Wh/kg)**	**Volumetric energy density (Wh/l)**	**Chemistry**	**Format**
Molicel INR-21700-M65A (Molicel, 2025)	322	943	NMC	cylindrical 21700
Odyssey ODP-ACEDINC (Odyssey Battery, 2026)	40	75	Lead-acid	prismatic
CATL Shenxing Plus (CATL, 2026)	205	-	LFP	prismatic

Table 1 Specifications of commercially available batteries in 2025

2.2 Heat development in lithium-ion cells

Heat generation in a lithium-ion cell arises from two main contributions: irreversible heat and reversible heat. Irreversible heat is associated with ohmic resistance, charge-transfer resistance, and concentration polarization, whereas reversible heat is linked to the entropy change of the electrochemical reactions and can either generate heat or absorb it depending on state of charge and operating direction. As current increases, the irreversible contribution becomes increasingly dominant because non-equilibrium losses grow with current and overpotential, while the relative influence of the reversible entropy term becomes smaller. For this reason, high-C-rate[1] operation generally leads to substantially higher total heat generation and stronger thermal gradients, making irreversible heat the principal term for thermal analysis under demanding charge and discharge conditions[5].

2.3 Importance of thermal management

Maintaining lithium-ion cells within an optimal temperature range is critical for performance, safety, and lifetime. A commonly accepted operating range is approximately 15–35 °C.

In practical applications, ambient conditions often deviate from this range. In addition, heat is continuously generated within the cell during charge and discharge due to internal resistance.

As an example, the Molicel INR-21700-M65A cell has a nominal capacity of 6.5Ah, nominal voltage of 3.6V, maximum discharge current of 26A, and a typical internal resistance of 25mΩ. The cell mass is 74.4g, and its specified operating temperature range is −30°C to 60°C.

The maximum electrical power output at nominal voltage can be estimated as:

$$P = U \times I \tag{1}$$

[1] C-rate denotes the charging or discharging current normalized to the nominal battery capacity. A rate of 1C corresponds to a current that would fully charge or discharge a battery in one hour. For example, a 5 Ah cell discharged at 3C would ideally be fully discharged in approximately 20 minutes.

which yields approximately 93.6W at the maximum discharge current.

Heat generation due to internal resistance can be estimated using:

$$P = R \times I^2 \quad (2)$$

At the maximum discharge current, this corresponds to approximately 16.9 W of internal heat generation.

Assuming adiabatic conditions, the resulting temperature rise can be estimated from:

$$Q = mc_p\Delta T \quad (3)$$

Using a specific heat capacity of $c_p = 1053 \text{Jkg}^{-1}\text{K}^{-1}$ [6], the cell temperature would increase from room temperature to 60 °C in approximately 3 minutes.

Electric hypercar Rimac Navera from 2020 has 6960 similar cells[7] which would scale to 118kW of heat generation. This simplified estimate illustrates the significance of heat generation and the necessity of effective thermal management.

Cycle life decreases when lithium-ion cells are charged at low temperatures. The primary mechanism responsible for this is lithium plating, which occurs when intercalation of lithium ions into the anode is kinetically limited. Under such conditions, lithium ions are reduced at the anode surface, forming metallic lithium instead of being intercalated into the electrode structure.

This process is largely irreversible and leads to capacity loss due to the consumption of active lithium. In addition, lithium plating can result in the formation of dendrites—needle-like metallic structures that may penetrate the separator, causing internal short circuits, localized heating, and potentially thermal runaway [8].

At elevated temperatures, a different degradation mechanism becomes dominant: growth of the solid electrolyte interphase (SEI). The SEI is a passivation layer formed on the anode surface during initial cycling due to electrolyte decomposition. While this layer is essential for stable battery operation, its continued growth during cycling and calendar aging consumes both electrolyte and active lithium, leading to capacity fade.

Elevated temperatures significantly accelerate SEI growth. An increase in SEI thickness also contributes to higher internal resistance by hindering lithium-ion transport. Experimental studies by Uitz [9] on commercial 18650 lithium-ion cells showed approximately 12.5% capacity loss after 500 cycles at room temperature, compared to 23.9% when cycled at 60 °C. Similar temperature dependence has been observed for calendar aging.

In extreme cases, excessive temperature rise can lead to thermal runaway (TR), a self-accelerating exothermic process that results in rapid temperature increase, gas release, and potential cell rupture. Experimental work by Golubkov [10] demonstrated that 18650 NMC cells can enter thermal runaway when heated to approximately 220 °C. Cells with internal defects may fail at even lower temperatures.

2.4 Heat transfer fundamentals

Heat transfer in engineering systems occurs through three fundamental mechanisms: conduction, convection, and thermal radiation [11]. In lithium-ion battery systems, heat transfer is typically dominated by conduction within solid materials and convection at external interfaces.

In conduction, thermal energy is transferred through a material due to microscopic interactions. In solids, this occurs primarily via lattice vibrations and, in metals, via free electrons. Heat flows from regions of higher temperature to lower temperature, opposite to the temperature gradient. This behaviour is described by Fourier's law:

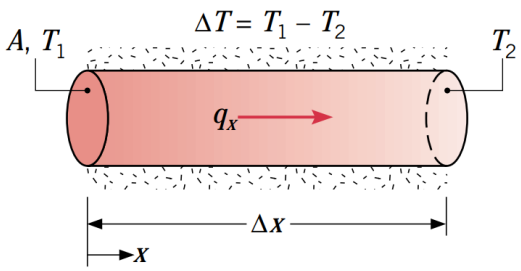

Figure 1: Thermal flux in a cylinder[11]

$$q_x = -kA\frac{\Delta T}{\Delta x} \tag{4}$$

where $q_x$is the heat transfer rate, k is the thermal conductivity ($W/m.K$), A is the cross-sectional area, and $\Delta T/\Delta x$is the temperature gradient. For most common materials k can be treated as a scalar (isotropic), but in anisotropic materials such as monocrystals the conductivity depends on direction and can be expressed with a tensor (e.g., single-crystal bismuth).

Thermal radiation involves the transfer of energy through electromagnetic waves and becomes significant at elevated temperatures. The radiative heat flux emitted by a surface is described by the Stefan–Boltzmann law:

$$E = \varepsilon\sigma T_s^4 \tag{5}$$

with ε the emissivity constant of the surface, Stefan-Boltzmann constant σ (σ=$5.67 \times 10^{-8}\ W/m^2\ \cdot K^4$), and T ($K$) the absolute surface temperature. In real situations actual net radiative heat flux depends on what the surroundings absorb and emit.

Last mechanism of heat transfer is convection which is a special case composed of two mechanisms. Energy is at first conducted from a solid source into a fluid at the boundary layer by conduction and then transported by the macroscopic motion of the fluid. Boiling water in a kettle is a simple example of convection. Main law describing convection is Newton's law of cooling. In the formula for convective heat flux q'' (W/m^2)

$$q'' = h\Delta T \tag{6}$$

h ($W/m^2.K$) is the heat transfer coefficient depending on the fluid medium, and ΔT (K) is the temperature difference between surface and the fluid.

2.5 Transverse heat flux sensor

2.5.1 Introduction

Heat flux $\vec{q}$ (W/m^2) through an object can be measured indirectly with the Fourier law (4) provided that the temperature difference, material properties, and geometry are known. This method introduces several measurement errors like the temperature and geometry measurement and has a relatively high response time due to thermal mass which makes it less suitable for dynamic measurements.

A more direct approach is provided by heat flux sensors (HFS), such as auxiliary-wall-type sensors. These devices typically consist of a thin plate with thermocouples arranged across its thickness. A temperature difference between the two surfaces generates an electromotive force (EMF) via the Seebeck effect, which can be related to the heat flux. This phenomenon is the same mechanism found in the common K-type thermocouples and is known as Seebeck effect [12]. In such sensors, the heat flux and the resulting electric field are aligned in the same direction [Figure 2 a].

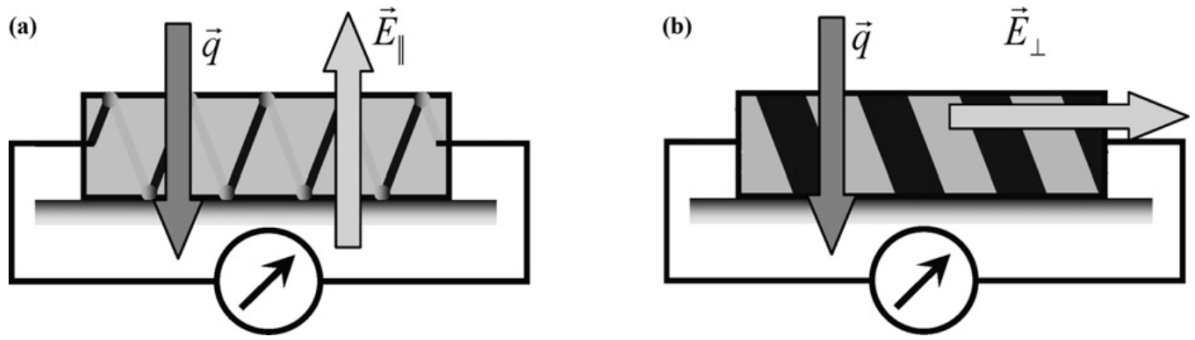

Figure 2 Thermocouple (a) and anisotropic transverse HFS (b) [12]

The transverse heat flux sensor (THFS) exploits materials with anisotropic thermal conductivity, electrical conductivity, and Seebeck coefficient. In anisotropic media these transport properties depend on direction relative to the principal material axes. When the sensor is oriented such that the applied heat flux is not aligned with the principal material axes, a transverse temperature gradient is generated. Through the transverse Seebeck effect, this results in an electric field perpendicular to the direction

of heat flux [Figure 2 b]. For a fixed geometry and material (after calibration), the resulting voltage is proportional to the heat flux and is expressed with equation (7) where $q"$ is heat flux through the sensor in W/m^2, E is output of the sensor in V, A is the sensor area in m^2, and the sensitivity S_0 $(\frac{V}{W})$.

$$q" = \frac{E}{A \times S_0} \tag{7}$$

The sensor used in this work was pre-calibrated, with an active area of 25mm^2 and sensitivity of 8.5 $\frac{mV}{W}$

First idea of measuring heat flow with anisotropic materials was proposed already by Faraday but it was L. Geiling who in 1947 proposed complete theory that electromotive force (EMF) could be induced but heat flux passing through a stack of alternating layers of two materials with different thermal conductivity and thermoelectric coefficients. For decades it has stayed a theory due to technical limitations. [13]

Same theory applies to HFSs made of anisotropic monocrystal materials. Bismuth and antimony are two examples from the limited pool of such materials. First THFS based on bismuth was made by N.P. Divin in the late 1990s. Sensors made of monocrystals have the advantage over the heterogeneous HFSs, of having volt-watt sensitivity independent from the temperature [12].

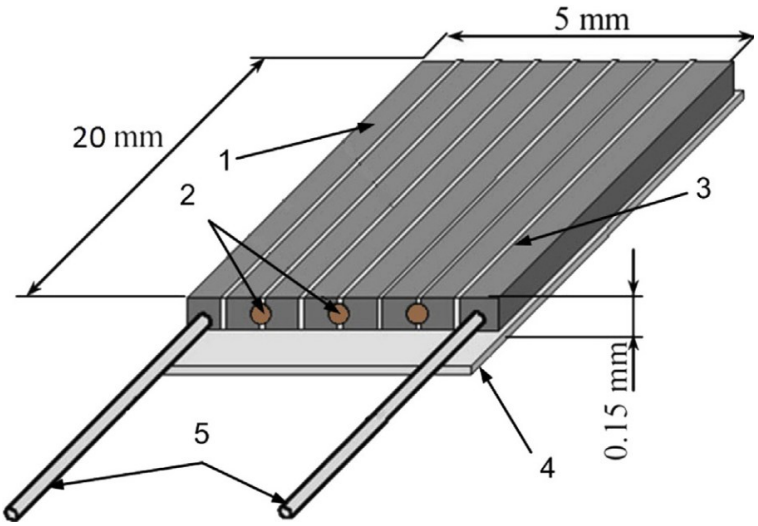

Figure 3: THFS: 1. thermoelement 2. solderings 3. insulator 4. mica base 5. output leads [12].

Schematic drawing [Figure 4] of a monocrystal THFS shows how contemporary sensors are build. Long slabs of anisotropic material are soldered together to achieve greater surface are in order to increase sensitivity as V/W output.

Time constant of a bismuth THFS is in order of 0.05ms as measured by Sapozhnikov, and Mityakov [13]. Later the time constant measurements were repeated, and the same authors find a mistake in the published results [12], they now confirmed the time constant to be around 10 ns. An interesting fact that they also learned is that thickness of the sensor does not influence the time constant. Authors replaced a 0.2mm sensor with thicker versions going up to 2.5mm and measured the same time constant. Current 0.2mm thickness of the sensors is limited by the manufacturing methods.

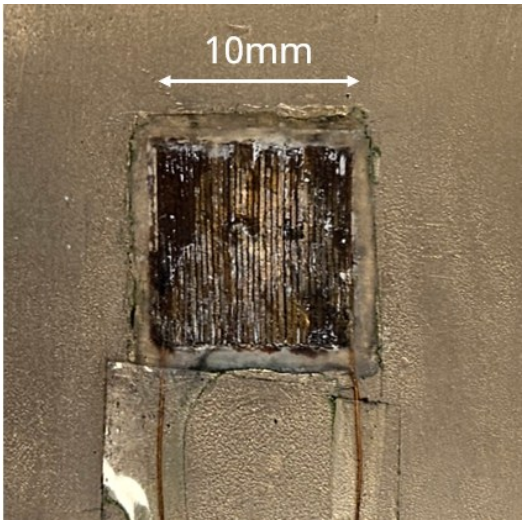

Figure 4: THFS Bismuth 10mm x 10mm

3 Experimental method

3.1 Experimental setup

The experiment was conducted using a Samsung INR21700-48X lithium-ion cell. According to the manufacturer datasheet[14], the cell has an internal resistance of 13 ± 5mΩ, a nominal capacity of 4.8Ah, and a mass of 68 ± 1.5g. This cell format was selected due to its high current capability (up to 21A and 43A respectively, depending on temperature and state of charge), wide availability, and common use in industrialised applications.

A total of eight K-type thermocouples were attached to the cell surface (see Figure 5). One thermocouple was placed on the negative terminal and one on the positive terminal. The remaining six sensors were distributed along the cylindrical surface in three axial positions, in radially opposite pairs. This configuration enables measurement of both axial and radial temperature gradients during operation. The bottom side of the cell was mounted in thermal contact with a cooling plate to provide a controlled heat sink boundary condition.

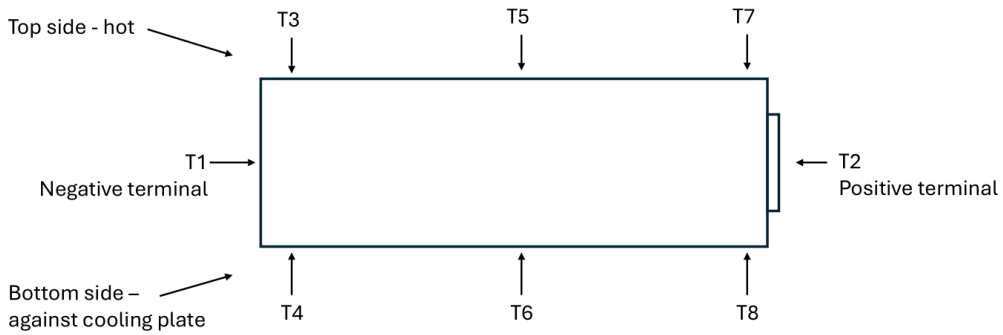

Figure 5 Thermocouples arrangement on the test cell

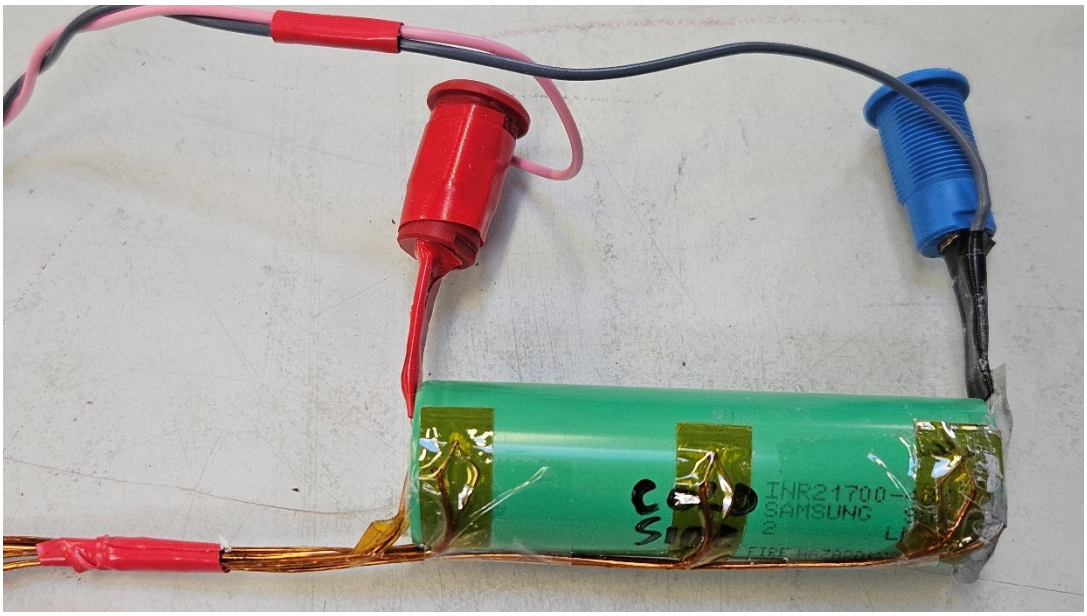

Figure 6: Cell with visible thermocouples, current terminals, and voltage sensing wires

An aluminium cooling plate was manufactured from two milled halves, incorporating an internal cooling channel. A small recess was machined to accommodate the THFS (see Figure 7).

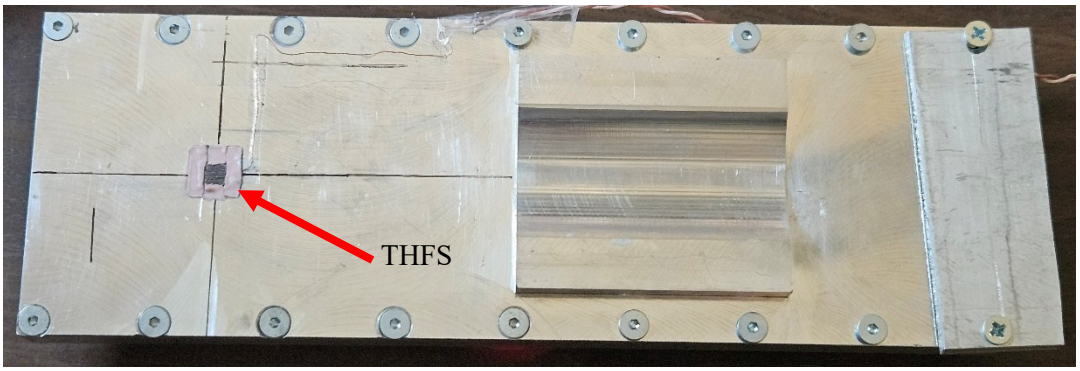

Figure 7: Cooling plate with the THFS on the left

A 3D-printed ABS bracket was mounted on top of the cooling plate to ensure consistent positioning of the cell. This V-shaped bracket serves to maintain a fixed and uniform distance between the cell and the cooling plate. It also functions as a mask with a

defined aperture, ensuring that the contact area between the cell and the plate remains well constrained. Aperture is 8.8mm wide.

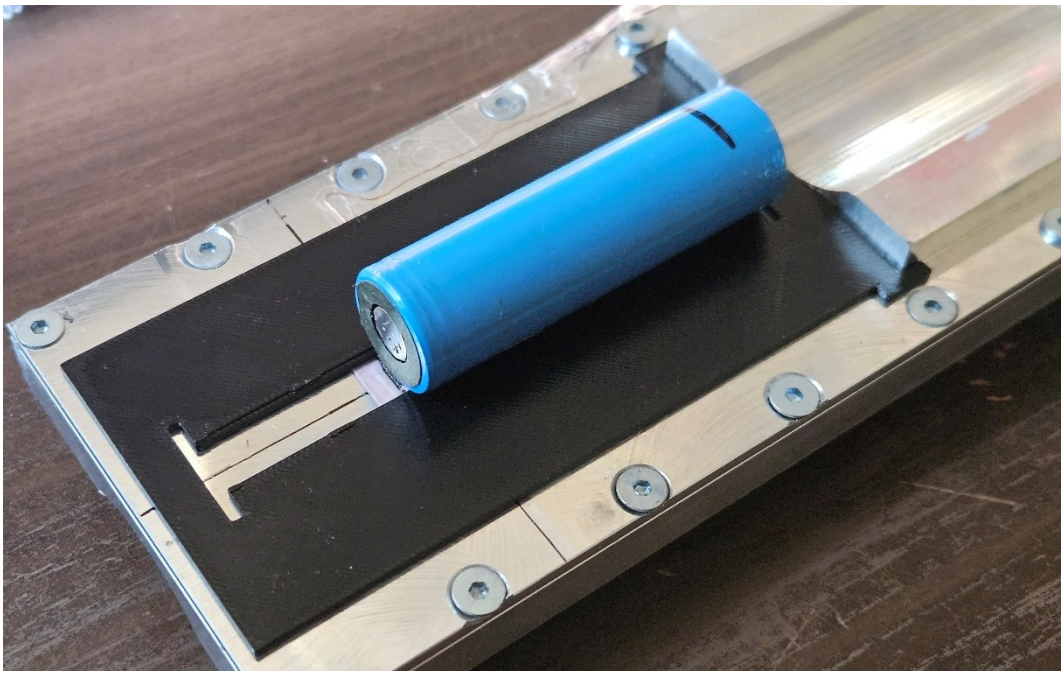

Figure 8: ABS bracket installed with cell in the "top" position

Finally, the cell was thermally insulated on all sides except the contact surface using a 20 mm thick layer of Finnfoam thermal insulation. The cooling plate surface was covered with a thermal pad, and a thermal gap filler was applied to improve contact conformity and reduce interfacial thermal resistance. To ensure mechanical stability and maintain consistent contact pressure during the experiment, a 1kg mass was placed on top of the cell.

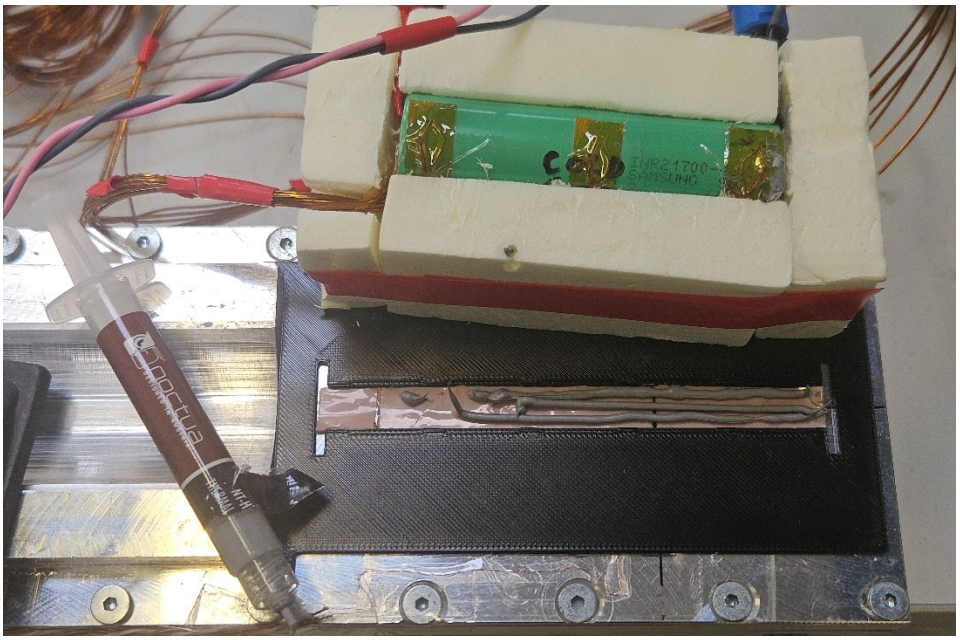

Figure 9: Cooling plate and cell with visible thermal interface materials before final assembly

3.2 Measurement procedure

The experiment consisted of measurements at three axial positions of the cell: a central position, a bottom position near the negative terminal, and a top position near the positive terminal.

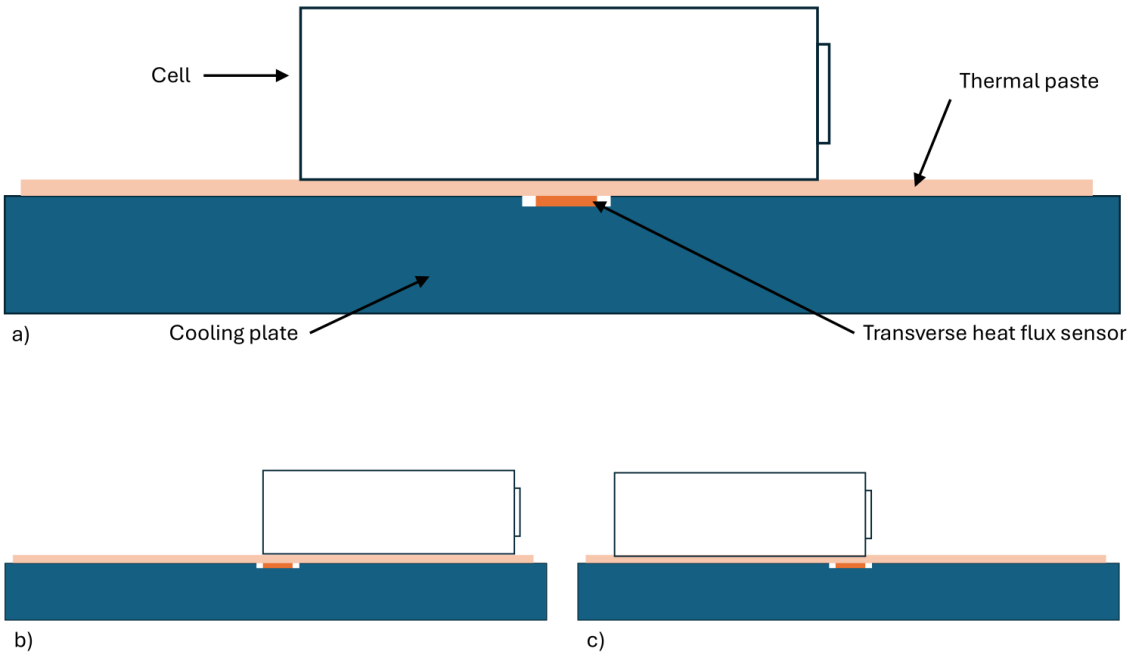

Figure 10 Three measurement positions: a) central, b) bottom, and c) top

The cooling plate was connected to a circulating thermostat (Lauda VC 5000) to provide controlled thermal boundary conditions. The coolant flow rate was set to approximately 2.56l/min, with an inlet temperature of 10.6°C. These parameters were maintained constant throughout all measurements to ensure repeatable cooling conditions.

The cell was first positioned centrally on the cooling plate, with the THFS located at the mid-height position of the cylindrical surface. The cell was cycled using a constant current of 9.6A for both charge and discharge. The cell was operated in short charge–discharge intervals around 40-50% state of charge to promote elevated heat generation and allow maximal currents. Each cycle consisted of a discharge to 3.3V followed immediately by a 30s constant-current charge. The full cycle duration was approximately 60s, and this sequence was repeated continuously until steady-state conditions were reached, defined by stable temperature and heat flux readings.

Subsequently, the cell was repositioned to the bottom axial location, such that the THFS was near the negative terminal. The same cycling procedure was repeated until thermal steady state was again achieved.

Finally, the cell was moved to the top axial position, placing the THFS near the positive terminal. After reaching thermal steady-state conditions, the experiment was terminated.

3.3 Data acquisition

Voltage signals from the THFS and thermocouple signals were both recorded using a Graphtec GL860 data logger. The instrument was configured for K-type thermocouples, and for voltage measurements with an input range of 0–20mV and 16-bit analog-to-digital conversion resolution. All channels were sampled at 2Hz to capture the thermal response during cycling.

For each measurement position, data were collected during continuous cycling until steady-state conditions were reached. Only the final three stable charge–discharge cycles prior to repositioning were used for analysis, corresponding to a total analysis window of approximately 180s per position.

Heat flux and temperature data were processed by averaging over these selected steady-state cycles. This approach reduced the influence of transient effects associated with individual charge–discharge transitions while preserving the quasi-steady thermal response of the system.

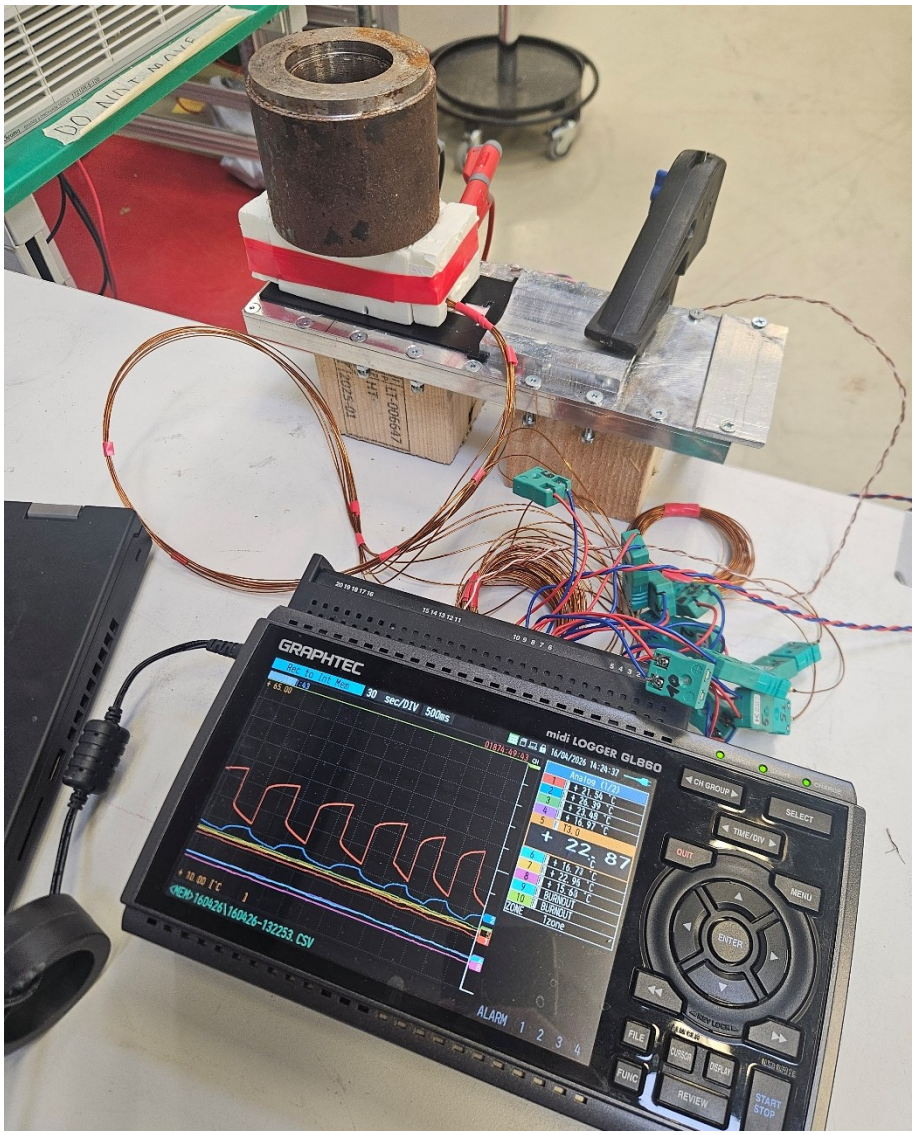

Figure 11 Measurement setup with visible datalogger, and cooling plate assembly

4 Results

4.1 Temperature and voltage results

As discussed previously, measurements were recorded continuously throughout the entire experiment, which spanned several hours. The complete dataset is provided in Appendix 1 .

For comparative analysis, three steady-state segments were extracted for each measurement position. Each segment had a duration of approximately 180s and was selected from the final phase of each measurement cycle, where the system response had stabilized. Linear regression was applied to each segment to determine the corresponding steady-state slope for further comparison between positions.
To facilitate direct comparison, the selected segments were placed consecutively and presented sequentially in a single chart, as shown in Figure 12.

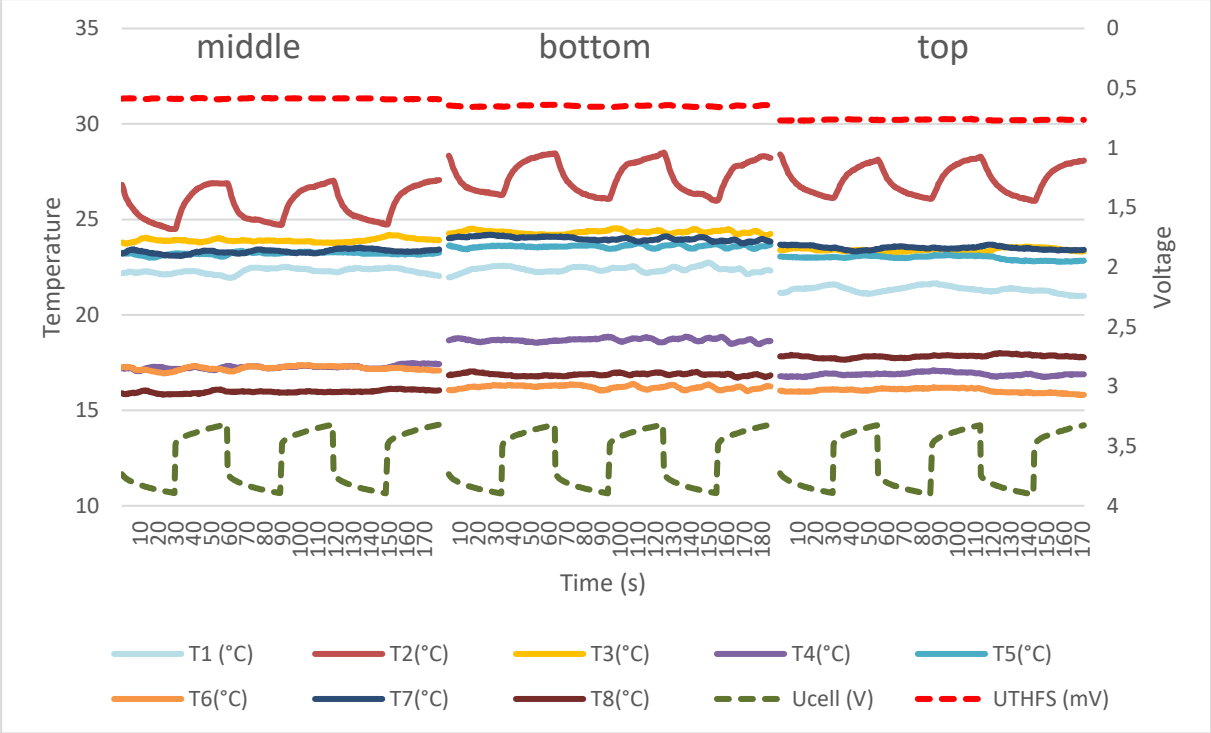

Figure 12 Chart of three consecutive measurements

To further simplify comparison, the measured quantities were averaged over the selected intervals for each position. The resulting mean values are presented in Table 2.

In addition, the temperatures recorded by all thermocouples (T1–T8) were averaged to obtain a representative bulk temperature of the cell.

Position	T1(°C)	T2(°C)	T3(°C)	T4(°C)	T5(°C)	T6(°C)	T7(°C)	T8(°C)	T_{avr}(°C)	U_{THFS} (mV)
middle	22.3	25.8	23.9	17.3	23.2	17.2	23.3	16.0	21.1	0.587
bottom	22.4	27.2	24.3	18.7	23.6	16.2	24.0	16.9	21.7	0.650
top	21.3	27.1	23.4	16.9	23.0	16.0	23.5	17.8	21.1	0.765

Table 2 Averaged measurements per position

The results show a relatively uniform average temperature across all positions, indicating that global thermal conditions of the cell remain consistent during the experiment. The resulting slope values were averaged across the three steady-state segments for each position and are summarized in Table 3. The temperature slopes are on the order of 10^{-4} to 10^{-3} °C/s, indicating that thermal drift during the selected intervals is negligible compared to measurement resolution, and the system can be approximated as quasi-steady-state. The slope of THFS signal exhibits values close to zero which is in-line with the temperature slopes.

Position	Slope T_{mean} (°C/s)	Slope U_{THFS} (V/s)
middle	9.60E-04	1.80E-05
bottom	2.40E-05	-1.20E-06
top	-3.10E-04	-9.17E-06

Table 3 Steady-state linear regression slopes

4.2 Heat flux results

Using the formula (6) we can calculate the heat flux through the sensor. As mentioned earlier A of the sensor is 25mm2 and the sensitivity S_0 is of 8,5 $\frac{mV}{W}$.

$$q" = \frac{E}{A \times S_0} \qquad (6)$$

Results of the calculations are presented in the Table 4.

Position	U_{THFS} (mV)	q'' (W/m2)	q_{sensor} (W)	$q_{normalized}$
middle	0,587	2765	0,069	0
bottom	0,650	3058	0,076	11%
top	0,765	3602	0,090	30%

Table 4 Heat flux results

The elevated heat flux measured near the terminals is consistent with localized ohmic heating in the current-collector/tab region. Because current constricts from the electrode foils into the narrow tab (see Figure 13), local current density and ohmic resistance increase, leading to higher irreversible heat generation near the terminals than in the electrode interior. This is a phenomenon known and studied in the industry [15] and has been tackled by invention of so called “tables” cell design where instead of one bottle-neck current tab, whole electrode edge is welded to the cell terminal [16].

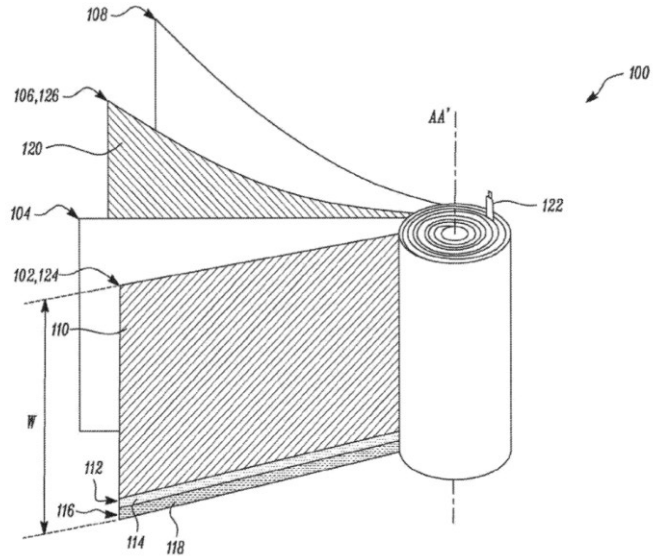

FIG. 1

Figure 13 Schematic picture of the cell jelly-roll with single current tab (detail 122) [16]

4.3 Approximation of heat development

Based on the heat flux results, an approximate estimation of total heat generation within the cell can be performed and compared with an independent electrical estimate based on internal resistance. As discussed earlier at higher C-rates ohmic loses become dominant [5] and for simplicity, reversible heat effects are neglected. Using the internal

resistance of 13 ± 5mΩ from the manufacturer datasheet and current of 9.6A that was used during the cycling, heat generation can be estimated using the formula $P = R \times I^2$, resulting in a range of 0.77 – 1.73W. Cell used in the experiment was not new and internal resistance tends to increase with decreasing state of health, hence possibility of even higher actual resistance and heat generation.

To obtain a comparable estimate from the experimental data, a weighted average of the measured heat flux values from Table 4 was used, assigning 80% contribution to the middle position and 10% to both the top and bottom positions. (That 1/1/8 ratio was chosen based on the internal construction of 21700 cells.) This weighting reflects the assumption that the central region represents the dominant portion of the cell surface. The resulting weighted heat flux was then multiplied by the effective contact area between the cell and the cooling plate (8.8 × 70 mm^2) to obtain an estimate of total heat transfer of 1.77W.

Heat estimate internal resistance	0.77 – 1.73W
Heat estimate THFS	1.77W

Table 5 Heat generation estimates

The agreement between the two estimates, within the uncertainty of the electrical method and the simplifying assumptions applied, indicates that the measured heat flux provides a realistic approximation of the total heat generation. This consistency supports the validity of the experimental approach and the use of THFS measurements for quantitative assessment of heat transfer at the cell–cooling interface.

4.4 Influence of Thermal Contact Conditions and Associated Uncertainty

Thermal contact resistance between the cell, thermal interface material (TIM), and cooling plate is a major source of uncertainty in heat flux measurements. In this study, a V-shaped fixture was used to ensure repeatable positioning of the 21700 cell and nominally constant TIM thickness across all measurements. A constant mechanical load of 1 kg was applied to maintain contact pressure.

The cooling plate temperature was actively controlled using a closed-loop system (Lauda VC 5000), ensuring consistent boundary conditions. The average cell temperature measured with six thermocouples showed minimal variation between measurement positions (21.1°C, 21.6°C, 21.1°C), indicating stable global thermal behaviour.

These factors suggest that large variations in overall thermal contact resistance between measurements are unlikely, although local variations at the sensor interface cannot be excluded. Therefore, absolute heat flux values are subject to systematic uncertainty, but relative spatial trends along the cell remain meaningful.

The observed ~30% increase in heat flux at the top position compared to the middle is unlikely to be explained solely by contact variation but should be interpreted as a semi-quantitative result due to remaining interface uncertainty.

5 Conclusion

This thesis investigated the spatial distribution of heat transfer from a cylindrical 21700 lithium-ion cell into a cooling plate using a transverse heat flux sensor. An experimental setup was developed in which the sensor was integrated in an actively cooled aluminium heat sink plate, enabling direct measurement of local heat flux at the cell–cooling interface during electrical cycling. By varying the axial position of the cell relative to the sensor, heat flux was resolved at three locations along the cell length: middle, bottom and top.

The results demonstrate a non-uniform distribution of heat transfer, with the central region of the cell having the lowest heat flux and higher flux near the cell terminals. This behaviour is consistent with the internal structure of cylindrical lithium-ion cells, where current collector near top and bottom contribute to more ohmic loses and heat generation. The measurements provide direct experimental evidence of spatial variation in heat transfer at the interface, which is typically not captured by conventional temperature-based methods.

A comparison between the experimentally derived heat transfer and an independent electrical estimate based on internal resistance showed close agreement within the expected uncertainty range. This indicates that the measured heat flux provides a realistic approximation of total heat generation and supports the validity of the experimental methodology.

The use of a THFS enabled direct, high-resolution measurement of heat flux with minimal disturbance to the thermal path and sufficient temporal response to capture dynamic behaviour. The results demonstrate that this approach is suitable for quantitative characterization of heat transfer at the cell–cooling interface.

The findings of this work provide experimental insight into the distribution of heat transfer in cylindrical lithium-ion cells and highlight the importance of considering spatial effects in the design of thermal management systems. The presented methodology can be applied in further studies for validation of thermal models and for evaluation of cooling strategies under realistic operating conditions.

Additionally, the sensor’s small thickness, rapid response time, and high sensitivity make it a promising candidate for integration as an online monitoring tool within battery packs. This application area remains relatively unexplored and may enable new developments in thermal monitoring and battery management systems.

References

[1] Beard, K. W., *Linden's Handbook of batteries*. McGraw Hill, 2019.

[2] Bloch, Didier; Priem, Thierry; Martinet, Sébastien; Ngô, Christian, *Li-Ion Batteries : Development and Perspectives*. EDP Sciences, 2022.

[3] Boddula, Rajender, *Rechargeable Batteries: History, Progress, and Applications*. Wiley, 2020.

[4] Addy, 'SONY Lithium Ion Batteries- Worlds First commercialized LiB 1991.', Battery Design. Accessed: Feb. 23, 2026. [Online]. Available: https://www.batterydesign.net/sony-lithium-ion-batteries-worlds-first-commercialized-lib-1991/

[5] Y. Xie, S. Shi, J. Tang, H. Wu, and J. Yu, 'Experimental and analytical study on heat generation characteristics of a lithium-ion power battery', *Int. J. Heat Mass Transf.*, vol. 122, pp. 884–894, Jul. 2018, doi: 10.1016/j.ijheatmasstransfer.2018.02.038.

[6] K. A. Murashko, A. V. Mityakov, J. Pyrhönen, V. Y. Mityakov, and S. S. Sapozhnikov, 'Thermal parameters determination of battery cells by local heat flux measurements', *J. Power Sources*, vol. 271, pp. 48–54, Dec. 2014, doi: 10.1016/j.jpowsour.2014.07.117.

[7] Nigel, '2020 Rimac Nevera', Battery Design. Accessed: May 14, 2026. [Online]. Available: https://www.batterydesign.net/2020-rimac-nevera/

[8] X. Huang *et al.*, 'Alternating current heating techniques for lithium-ion batteries in electric vehicles: Recent advances and perspectives', *J. Energy Chem.*, vol. 96, pp. 679–697, Sep. 2024, doi: 10.1016/j.jechem.2024.05.027.

[9] M. Uitz *et al.*, 'Aging of Tesla's 18650 Lithium-Ion Cells: Correlating Solid-Electrolyte-Interphase Evolution with Fading in Capacity and Power', *J. Electrochem. Soc.*, vol. 164, pp. A3503–A3510, Nov. 2017, doi: 10.1149/2.0171714jes.

[10] A. W. Golubkov *et al.*, 'Thermal-runaway experiments on consumer Li-ion batteries with metal-oxide and olivin-type cathodes', *RSC Adv*, vol. 4, no. 7, pp. 3633–3642, 2014, doi: 10.1039/C3RA45748F.

[11] Incropera, Frank P.; DeWitt, David P.; Bergman, Theodore L.; Lavine, Adrienne S., *Fundamentals of Heat and Mass Transfer*. John Wiler & Sons, 2006.

[12] A. V. Mityakov, S. Z. Sapozhnikov, V. Y. Mityakov, A. A. Snarskii, M. I. Zhenirovsky, and J. J. Pyrhönen, 'Gradient heat flux sensors for high temperature environments', *Sens. Actuators Phys.*, vol. 176, pp. 1–9, Apr. 2012, doi: 10.1016/j.sna.2011.12.020.

[13] S. Z. Sapozhnikov, V. Y. Mityakov, and A. V. Mityakov, 'Bismuth-Based Gradient Heat-Flux Sensors in Thermal Experiment', *High Temp.*, vol. 42, no. 4, pp. 629–638, 2004, doi: 10.1023/B:HITE.0000039993.76288.01.

[14] 'TDS Samsung-INR21700-48X'. Samsung, Apr. 28, 2020.

[15] P. Taheri, A. Mansouri, B. Schweitzer, M. Yazdanpour, and M. Bahrami, ‘Electrical Constriction Resistance in Current Collectors of Large-Scale Lithium-Ion Batteries’, *J. Electrochem. Soc.*, vol. 160, no. 10, pp. A1731–A1740, 2013, doi: 10.1149/2.041310jes.

[16] K. Tsuruta, M. E. DERMER, and R. Dhiman, ‘A cell with a tabless electrode’, WO2020096973A1, May 14, 2020 Accessed: Apr. 26, 2026. [Online]. Available: https://patents.google.com/patent/WO2020096973A1/en

Appendices

Appendix 1 All measurements